Comparison of Fourier and model-based estimators in single-mode multi-axial interferometry

E. Tatulli, J. B. Lebouquin

Mon. Not. R. Astron. Soc. **368,** 1159–1168 (2006) doi:10.1111/j.1365-2966.2006.10203.x

Comparison of Fourier and model-based estimators in single-mode multi-axial interferometry

E. Tatulli⋆ and J.-B. LeBouquin⋆

Laboratoire d'Astrophysique, Observatoire de Grenoble, 38041 Grenoble cedex, France

Accepted 2006 February 10. Received 2006 February 8; in original form 2005 April 25

ABSTRACT

There are several solutions to code the signal arising from optical long-baseline multi-aperture interferometers. In this paper, we focus on the non-homothetic spatial coding scheme (multi-axial) with the fringe pattern coded along one dimension on one detector (all-in-one). After describing the physical principles governing single-mode interferometers using that sort of recombination scheme, we analyse two different existing methods that measure the source visibility. The first technique, the so-called Fourier estimator, consists of integrating the high-frequency peak of the power spectral density of the interferogram. The second method, the so-called model-based estimator, has been specifically developed for the Astronomical Multi-BEam combineR (AMBER) instrument of the Very Large Telescope Interferometer (VLTI) and deals with directly modelling the interferogram recorded on the detector. Performances of both estimators are computed in terms of the signal-to-noise ratio (S/N) of the visibility, assuming that the interferograms are perturbed by photon and detector noises. Theoretical expressions of the visibility S/N are provided, validated through numerical computations and then compared. We show that the model-based estimator offers up to 5 times better performances than the Fourier one.

Key words: instrumentation: interferometers – methods: data analysis – techniques: interferometric.

1 INTRODUCTION

The next challenge of long-baseline optical interferometry is to commonly perform direct imaging of the observed source, analogous to the way it is done in radio-interferometry (Högbom 1974) or in infrared aperture masking (Tuthill, Monnier & Danchi 2000). After the first promising results obtained with the Cambridge Optical Aperture Synthesis Telescope (COAST) (Baldwin et al. 1996; Young et al. 2000), Navy Prototype Optical Interferometer (NPOI) (Hummel 1998) and Infrared Optical Telescope Array (IOTA) (Monnier et al. 2004a), such a technique should soon move one step forward with the operating of the Astronomical Multi-BEam combineR (AMBER) instrument (Petrov et al. 2000), the three beam recombiner of the Very Large Telescope Interferometer (VLTI). From the beginning of 2005, AMBER will indeed take full benefit of the unique combination of the great sensitivity of large aperture telescopes and the spatial frequency coverage provided by the VLTI, even though it will require multiple nights of observing to be able to restore consistent images (Thiébaut, Garcia & Foy 2003; Tatulli et al. 2004a). Then, in less than a decade, huge improvements are expected to be accomplished with second generation instruments of the VLTI that will enable snapshot imaging by using four, six or even eight telescopes simultaneously (e.g. Malbet et al. 2004).

One critical point in the design of future interferometric imaging instruments is the choice of the beam recombination scheme, which can become particularly complex, especially when dealing with multi-aperture ($N_{\rm tel} \geqslant 3$) interferometers. Following the solution that has been chosen for the AMBER instrument, we investigate the properties of a single-mode non-homothetic spatial coding scheme (from now on 'multi-axial') with the fringe pattern in the same spatial dimension on the same detector (from now on 'all-in-one'). In other words, interferograms are obtained by mixing together all the input beams arising from the different telescopes, thanks to output pupils arranged along one single dimension (see Fig. 1). We analyse the ways to estimate the source visibility from such interferograms.

Indeed, single-mode multi-axial all-in-one recombination appears particularly well suited in the framework of interferometric imaging. First, it is the simplest and most compact way to recover information arising from all the baselines. Moreover, it provides a better transmission than Michelson recombination schemes (i.e. temporal coding) because it makes use of fewer mirrors and beam splitters for the same given number of input pupils. In addition, the number of pixels required to code the signal is also smaller, driving to higher limiting magnitudes (Lebouquin et al. 2004). Furthermore, the remarkable spatial filtering properties of single-mode waveguides allow to change the phase corrugations of the

⋆E-mail: lastname@obs.ujf-grenoble.fr

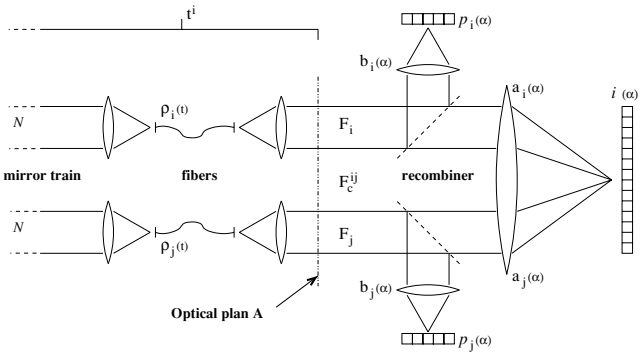

Figure 1. Sketch of a multi-axial all-in-one single-mode interferometer. t^i denotes the total 'static' transmission from the ith telescope aperture to the optical plane A (i.e. mirrors, delay line, transmission of the ith fibre, ...), whereas ρ^i takes into account the 'dynamical' transmission, i.e. the coupling coefficient of the ith fibre. $i(\alpha)$ is the interferogram. $p^i(\alpha)$ and $p^j(\alpha)$ are the photometric channels. The photometric fluxes F^i, F^j and the coherent flux F_c^{ij} are defined in the optical plane A. $a^i(\alpha)$ and $b^i(\alpha)$ are respectively the detected beams in the interferometric and photometric channels. In other words, $a^i(\alpha)$ and $b^i(\alpha)$ are the transmission factor between the photometric flux and the interferometric and photometric channels, respectively. Note that the definition of $a^i(\alpha)$ and $b^i(\alpha)$ includes the transmission of the beam splitter.

incoming turbulent wavefront into intensity fluctuations at the output of the fibres. In other words, only one fraction of the source flux, the so-called coupling coefficient, which depends on the Strehl ratio of the pupil apodized by the fibre single mode (Coudé du Foresto et al. 2000), remains in the interferogram. However, the very advantageous counterpart is that the shape of the interferogram is entirely deterministic, i.e. the form of the peaks in the Fourier plane is fixed, and the fringe pattern is fully determined by two free parameters, its amplitude and its phase.

Before the advent of single-mode interferometers and in order to overcome the problem of the turbulence, Roddier & Léna (1984) proposed to estimate the visibility in the Fourier plane from the integration of the high-frequency peak of the long exposure power spectral density of the interferogram. Then Coudé Du Foresto, Ridgway & Mariotti (1997), in a natural way, used the same estimator to compute the visibility arising from the Fiber Linked Unit for Recombination (FLUOR) experiment, the first interferometer making use of single-mode waveguides. In multi-axial coding, we can furthermore take advantage of the deterministic nature of the interferogram shape to perform model fitting techniques. It was though only recently, namely for the AMBER instrument, that this property was used to estimate the visibility, by fitting the fringe pattern (its phase and its amplitude) in the detector plane (Millour et al. 2004).

In this paper, we recall in Section 2 the general formalism of multi-axial all-in-one recombination, i.e. the equation governing the interferogram, as well as the two techniques currently used to estimate the visibility. As mentioned above, the first technique, the so-called Fourier estimator, integrates the high-frequency peak of the power spectral density of the interferogram, whereas the second one, the so-called model-based estimator, directly models the interferogram in the detector plane. For both estimators, theoretical expressions of the signal-to-noise ratio (S/N) of the visibility are provided. In Section 3, those expressions are validated thanks to numerical simulations of noisy interferograms. Then in Section 4 both estimators are compared, from a formal point of view and in terms of relative performances. The influence of instrumental parameters is investigated as well, with a special emphasis regarding the choice of the width of the reading window of the detector. The presence of an atmospheric piston that blurs the fringes has not been taken into account in this analysis. Indeed, regardless of the chosen estimator, its effect results in an attenuation of the squared visibility (Colavita 1999), and the sensitivity of both estimators to this point is the same.

This paper is the first part of our study on multi-axial all-in-one recombination. In a second paper (Lebouquin & Tatulli, in preparation), we analyse in which way such a recombination scheme allows to optimize the visibility S/N thanks to specific geometric configuration of the output pupils.

2 GENERAL FORMALISM

Fig. 1 sketches the principle of multi-axial recombination in waveguided interferometers. The light arising from the ith telescope is filtered by a single-mode fibre to convert phase fluctuations of the corrugated wavefront into intensity fluctuations. The fraction of light ρ^i entering the fibre is called the coupling coefficient (Shaklan & Roddier 1988) and depends on the Strehl ratio of the apodized pupil (Coudé du Foresto et al. 2000). Making use of a beam splitter, one part of the light is selected to estimate the photometry, thanks to dedicated photometric channels. The remaining part of the light is recombined with the beam coming from the jth telescope to form fringes. The coding frequency of the fringes f^{ij} is fixed by the separation of the output pupils, which are arranged along one dimension.

When only the ith beam is lit, the signal recorded on the interferometric channel is the photometric flux F^i spread on the intensity mode pattern $a^i(\alpha)$, i.e. the diffraction pattern of the ith output pupil weighted by the single mode of the fibre. α is the angular variable in the image plane. F^i results in the source photon flux N attenuated by the total transmission of the instrument, i.e. the product of the 'static' transmission t^i and the coupling coefficient ρ^i of the single-mode fibre:

$$F^i = N t^i \rho^i. \tag{1}$$

When beams i and j are lit simultaneously, the coherent addition of both beams results in an interferometric component superimposed onto the photometric continuum. The interferometric part, i.e. the fringes, arises from the amplitude modulation of the coherent flux $F^{ij}{}_c$ at the coding frequency f^{ij}. The coherent flux is the geometrical product of the photometric fluxes, weighted by the visibility:

$$F_c^{ij} = 2N\sqrt{t^i t^j}\sqrt{\rho^i \rho^j} V^{ij} \mathrm{e}^{\mathrm{i}(\Phi^{ij} + \phi_p^{ij})}, \tag{2}$$

where $V^{ij}\mathrm{e}^{\mathrm{i}\Phi^{ij}}$ is the complex modal visibility (Mège, Malbet & Chelli 2001) and ϕ_p^{ij} takes into account a potential differential atmospheric piston. Note that, strictly speaking, the modal visibility is not the source visibility. Rigorously, the modal visibility depends on the convolution between the source visibility and the telescope transfer function, which is atmosphere dependent in the optical range. As such, the modal visibility is biased both by the geometric antenna-lobe effect (the object is multiplied by the telescope point spread function, as commonly known in radio-astronomy) and by the turbulence. When the object is unresolved by one single telescope however, the modal visibility can be fairly approximated by the object one (Tatulli & Chelli 2005) and its estimation is robust (stable to the level of 1 per cent or less) to a change of atmospheric conditions during the calibration process (Tatulli et al. 2004b). In any case, a further study of the relationship between the modal visibility and the source visibility is beyond the scope of this paper, and further

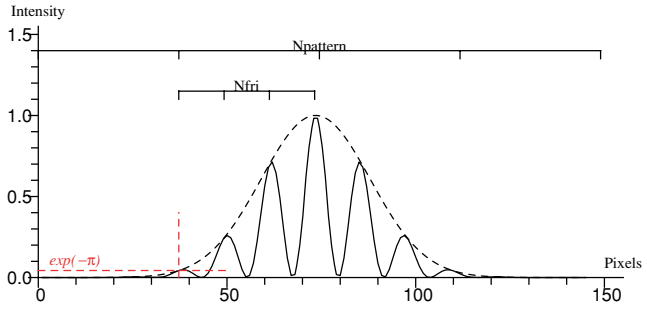

Figure 2. Image of a typical interferogram at the output of a multi-axial all-in-one recombiner. Here is shown a two-beam recombination with instrumental contrast set to 1. The fringes are weighted by the intensity mode pattern (dashed line). $N_{\rm pattern}$ indicates the width of the detector reading window, the width of one mode pattern being defined as the interval between the top of the Gaussian mode and where the amplitude of the Gaussian mode has decreased by a factor exp $(-\pi)$. This definition has been chosen so that this width corresponds to half of the first lobe of the Airy pattern in the case of pupils which are not weighted by the first mode of single-mode fibres. $N_{\rm fri}$ refers to the number of fringes in one mode pattern. This term is fixed by the distance between the output pupils.

information can be found in the papers mentioned above. Here, we consider our observable to be the modal visibility.

Such an analysis can be done for each pair of telescopes available in the interferometer. As a result, the interferogram recorded on the detector can be written in the general form:

$$i(\alpha) = \sum_{i}^{N_{\rm tel}} a^i(\alpha) F^i + \sum_{i<j}^{N_{\rm tel}} \sqrt{a^i(\alpha) a^j(\alpha)} C_B^{ij}(\alpha) \mathrm{Re}\left[F_{\rm c}^{ij} \mathrm{e}^{\mathrm{i}(2\pi\alpha f^{ij} + \phi_{\rm s}^{ij}(\alpha) + \Phi_B^{ij}(\alpha))}\right], \tag{3}$$

where $\phi_{\rm s}^{ij}(\alpha)$ is the instrumental phase taking into account a possible misalignment and/or differential phase between the beams $a^i(\alpha)$ and $a^j(\alpha)$. C_B^{ij} and $\Phi_B^{ij}(\alpha)$ are respectively the loss of contrast and the phase shift due to diffusion and polarization effects,[1] which may not be homogeneous along the fringe pattern. Fig. 2 gives an example of a multi-axial all-in-one interferogram in the two-telescope case.

Thanks to the photometric channels, the number of photoevents $p^i(\alpha)$ coming from each telescope can be estimated independently:

$$p^i(\alpha) = F^i b^i(\alpha), \tag{4}$$

where $b^i(\alpha)$ is the detected beam in the ith photometric channel.

We can notice from equations (1) and (2) that the estimator of the squared modal visibility $|\widetilde{V^{ij}}|^2$ results in the ratio between the squared coherent flux and the photometric fluxes. Using the previous definitions, we can set a generic form of the estimator as follows:

$$|\widetilde{V^{ij}}|^2 = \frac{\langle |F_{\rm c}^{ij}|^2 \rangle}{\langle 4 F^i F^j \rangle}. \tag{5}$$

Note that $\langle\, |F_{\rm c}^{ij}|^2 \rangle$ is computed instead of $\langle F_{\rm c}^{ij} \rangle$ because, in the absence of fringe tracking, the random atmospheric differential piston $\phi_{\rm p}^{ij}$ totally blurs the coherent signal. It now remains to estimate F^i and $F_{\rm c}^{ij}$ from the interferogram.

[1] Assuming a non-polarized incoming light.

2.1 Fourier estimator: integrating the power spectral density

In the Fourier space, the interferogram defined by equation (3) takes the form of the sum of photometric and interferometric peaks. The photometric peaks are centred at the zero spatial frequency, whereas the interferometric peaks $\widehat{M}_+^{ij}(f)$ are located at their respective spatial coding frequency f^{ij}, their counterpart $\widehat{M}_-^{ij}(f)$ being in the negative spatial frequency domain. This method in the Fourier space requires that (i) the photometric peaks and the interferometric peaks are not overlapping, and (ii) the high-frequency peaks are not overlapping one another. If these conditions are fulfilled, the squared coherent flux can be estimated by computing the integral of the power spectral density $|\widehat{M}_+^{ij}(f)|^2$ (Roddier & Léna 1984; Conan 1994), over its frequency support, i.e. $[f^{ij} - D/\lambda,\ f^{ij} + D/\lambda]$ where D is the diameter of the output pupil. From the definition of the coherent flux and using the Parseval equality, one obtains

$$\int |\widehat{M}_+^{ij}(f)|^2 \mathrm{d}f = \left|F_{\rm c}^{ij}\right|^2 \frac{\int {C_B^{ij}}^2(\alpha) a^i(\alpha) a^j(\alpha)\, \mathrm{d}\alpha}{4}. \tag{6}$$

The photometric flux is easily computed from the photometric channel (see equation 4):

$$\widehat{P}^i = F^i \int b^i(\alpha)\, \mathrm{d}\alpha. \tag{7}$$

Then the estimation of the fringe contrast C^{ij} is written as

$$|\widetilde{C^{ij}}|^2 = \frac{\left\langle \int |\widehat{M}_+^{ij}(f)|^2 \mathrm{d}f \right\rangle}{\langle \widehat{P}^i \widehat{P}^j \rangle} = |\widetilde{V^{ij}}|^2 \times C_{\rm r}^2, \tag{8}$$

with

$$C_{\rm r}^2 = \frac{\int {C_B^{ij}}^2(\alpha) a^i(\alpha) a^j(\alpha)\, \mathrm{d}\alpha}{\int b^i(\alpha)\, \mathrm{d}\alpha \int b^j(\alpha)\, \mathrm{d}\alpha} \tag{9}$$

being the instrumental contrast of the recombiner that depends on the contrast loss due to polarization effects, on the alignment of the beams $a^i(\alpha)$ and $a^j(\alpha)$, and on the flux ratio between the interferometric and the photometric channels. Note that the power spectral density of the interferogram has to be properly unbiased from photon and detector noise (Perrin 2003).

2.2 Model-based estimator: modelling the interferogram

The model-based estimator has been introduced for the first time in the data reduction process of the AMBER instrument (Millour et al. 2004). It consists of modelling the interferogram thanks to a priori knowledge of the instrument. The purpose of such a signal processing is twofold: (i) to develop optimized algorithms in terms of performances of the instrument, i.e. the S/N of the visibility; and (ii) in contrast to the Fourier estimator, to authorize high-frequency peak overlapping when dealing with multibeam ($N_{\rm tel} > 3$) recombination, thus allowing to code the interferogram on fewer pixels. This second point is beyond the scope of this paper. Let us just mention here that plainly choosing the different coding frequencies is crucial to optimizing the design of the multibeam recombiner making use of integrated optics. This is especially true in the case of imaging instruments such as VITRUV (Lebouquin et al. 2004) that are recombining four beams or more, as is shown in our second paper on the subject (Lebouquin & Tatulli, in preparation).

A full description of this estimator can be found in Millour et al. (2004). We only recall here the basics principles. To model the signal on the detector, equation (3) has to be rewritten in its sampled

version, where k stands for the pixel number, between 1 and $N_{\rm pix}$:

$$i_k = \sum_i^{N_{\rm tel}} F^i a_k^i + \sum_{i<j}^{N_{\rm tel}} c_k^{(i,j)} R^{ij} + d_k^{(i,j)} I^{ij}, \tag{10}$$

with

$$c_k^{(i,j)} = \frac{C_B^{ij}(k)\sqrt{a_k^i a_k^j}}{\sqrt{\sum_k {C_B^{ij}}^2(k) a_k^i a_k^j}} \times \cos\left[2\pi\alpha_k f^{ij} + \phi_{\rm s}^{ij}(k) + \Phi_B^{ij}(k)\right] \tag{11}$$

and

$$R^{ij} = \sqrt{\sum_k {C_B^{ij}}^2(k) a_k^i a_k^j}\,{\rm Re}\left[F_{\rm c}^{ij}\right], \tag{12}$$

$d_k^{(i,j)}$ and I^{ij} being the quadratic counterpart of $c_k^{(i,j)}$ and R^{ij}, respectively. $c_k^{(i,j)}$ and $d_k^{(i,j)}$ are called the carrying waves of the signal at the coding frequency f^{ij}, because they 'carry' (in terms of amplitude modulation) R^{ij} and I^{ij}, which are directly linked to the complex coherent flux. Furthermore, the photometric fluxes are still computed from the photometric channels (see equation 7):

$$p^i = F^i \sum_k b_k^i. \tag{13}$$

F^i and $F_{\rm c}^{ij}$ are then jointly estimated from the photometry (p^i) and the interferogram (i_k) by resolving a set of ($N_{\rm pix} + N_{\rm tel}$) linear equations with ($2N_b + N_{\rm tel}$) unknowns [N_b being the number of pairs of telescopes, i.e. $N_b = N_{\rm tel}(N_{\rm tel}-1)/2$]:

$$\begin{bmatrix} i \\ p \end{bmatrix} = [\mathbf{C}] \begin{bmatrix} R \\ I \\ F \end{bmatrix}, \tag{14}$$

where the matrix $\mathbf{C}$ takes the detailed form

$$\overbrace{\begin{pmatrix} .. & c_1^{(i,j)} & .. & .. & d_1^{(i,j)} & .. & .. & a_1^i & .. \\ | & : & | & | & : & | & | & : & | \\ .. & c_{N_{\rm pix}}^{(i,j)} & .. & .. & d_{N_{\rm pix}}^{(i,j)} & .. & .. & a_{N_{\rm pix}}^i & .. \\ 0 & .. & 0 & 0 & .. & 0 & \sum b_k^1 & .. & 0 \\ | & \ddots & : & | & \ddots & | & | & \ddots & | \\ 0 & .. & 0 & 0 & .. & 0 & 0 & .. & \sum b_k^{N_{\rm tel}} \end{pmatrix}}^{N_b \quad N_b \quad N_{\rm tel}}. \tag{15}$$

The matrix $\mathbf{C}$ entirely characterizes the instrument. It depends on the shape of the detected beams a_k^i, b_k^i and on the carrying waves $c_k^{(i,j)}$, $d_k^{(i,j)}$ that hold information about the interferometric beam $\sqrt{a_k^i a_k^j}$, the coding frequencies f^{ij} and the instrumental differential phases $\phi_{\rm s}^{ij}$, and the polarization state within C_B^{ij} and Φ_B^{ij}. Such quantities can be calibrated in a laboratory, hence they are assumed to be perfectly known. The calibration procedure is fully described by Millour et al. (2004). $\mathbf{C}$ has to be inverted in order to solve the system. In the AMBER experiment, the generalized inverse of $\mathbf{C}$ has been called the Pixel To Visibility Matrix (P2VM), because it enables to compute the visibility of the fringes from the measurements on the detector. The estimation of the contrast is written as

$$\widetilde{|C^{ij}|^2} = \frac{\left\langle R^{ij2}\right\rangle + \left\langle I^{ij2}\right\rangle}{\left\langle p^i p^j\right\rangle} = \widetilde{|V^{ij}|^2} \times C_{\rm r}^2. \tag{16}$$

$C_{\rm r}^2$ is still the squared instrumental contrast

$$C_{\rm r}^2 = \frac{\sum_k {C_B^{ij}}^2(k) a_k^i a_k^j}{\sum_k b_k^i \sum_k b_k^j} \tag{17}$$

with the same definition as in equation (9). Note that the quantity $R^{ij2} + I^{ij2}$ has to be properly unbiased, like the power spectral density in the Fourier plane.

Table 1. Covariances for both estimators.

Fourier estimator	Model-based estimator
Cov $(\lvert F_{\rm c}^{ij}\rvert^2, F^i F^j) = 0$	Cov $(\lvert F_{\rm c}^{ij}\rvert^2, F^i F^j) \neq 0$
Cov $(F^i, F^j) = 0$	Cov $(F^i, F^j) \neq 0$

2.3 S/N of the modal visibility

Using second-order expansion of Papoulis (1984), we derive from equation (5) the relative error (i.e. the inverse of the S/N) of the squared visibility:

$$\mathcal{E}^2(|V^{ij}|^2) = \frac{\sigma^2(\left|F_{\rm c}^{ij}\right|^2)}{\overline{\left|F_{\rm c}^{ij}\right|^2}^2} + \frac{\sigma^2(F^i)}{\overline{F^i}^2} + \frac{\sigma^2(F^j)}{\overline{F^j}^2} + 2\frac{{\rm Cov}(F^i, F^j)}{\overline{F^i F^j}} - 2\frac{{\rm Cov}\left(\left|F_{\rm c}^{ij}\right|^2, F^i F^j\right)}{\overline{\left|F_{\rm c}^{ij}\right|^2}\,\overline{F^i F^j}}. \tag{18}$$

The main difference between both approaches lies in the following remark: in the case of the Fourier estimator, the coherent and photometric fluxes are directly estimated from the measurements, each *independently*, whereas in the case of the model-based estimator, the coherent and photometric fluxes are *jointly* reconstructed from the measurements by way of computation of the P2VM matrix, and are therefore correlated. As a result, we have the situations presented in Table 1.

Detailed computation of equation (18) is given in Appendix A for both estimators, assuming that the interferogram is corrupted by photon and detector noise. Atmospheric noise is neglected here because it has been shown in Tatulli et al. (2004b) that, in presence of modal filtering (and in contrast to multispeckle interferometry; Goodman 1985), speckle noise is the dominant noise in the case of very bright sources (negative magnitudes) only, and is therefore marginally relevant. Furthermore, we did not take into account in these computations the effect of the atmospheric piston because it only results in the attenuation of the squared visibility, the sensitivity of both estimators to this specific point being the same.

In next section, we propose to simulate the estimation of the modal visibility from multi-axial recombination and to validate our theoretical calculations. Then we compare the performances of both estimators.

3 VALIDATION OF THE THEORETICAL EXPRESSIONS

In order to validate our theoretical expressions derived in the previous section, we perform statistical simulations of noisy interferograms. For the sake of simplicity, we assume from now on a two-telescope interferometer. Note however that the validity of our theoretical approach has been also checked for an increasing number of telescopes. Moreover, a deep analysis of multibeam ($\geqslant$3) recombination is proposed in our second paper on the subject (Lebouquin & Tatulli, in preparation).

Following the formalism of Section 2, the interferogram arising from multi-axial all-in-one recombination is entirely defined by the following parameters.

(i) The shape of $a(\alpha)$, which is assumed to be the same for each beam. It arises from the inverse Fourier Transform of the autocorrelation of the output pupil of diameter D. To take into account the weighting of the single-mode fibre, we assumed a Gaussian shape with a pupil stop of width D (that is a convolution by a Bessel function in the detector plane). As a result, the low- and high-frequency peaks have truncated Gaussian shapes with a base width of $2D/\lambda$. We consider that the photometry is recorded on one pixel.

(ii) The number of fringes $N_{\rm fri}$ in the interference pattern for the lowest coding frequency. It is defined as the distance between the closest output pupils in D/λ units (see Fig. 2). We choose here $N_{\rm fri} = 2$.

(iii) The number of pixels per fringe $N_{\rm pf}$ to code the interferogram. It must be chosen such that it fulfils the Shannon criteria for the highest frequency coding $f_{\rm max}$ of the carrying waves. If it is written under the form $f_{\rm max} = \beta D/\lambda$, then the number of pixels must verify $N_{\rm pf} \geqslant 2\beta$. For the two-telescope case considered here, we arbitrarily set $N_{\rm pf} = 2.5$.

(iv) The width of the detector reading window $N_{\rm pattern}$ that fixes the total number of fringes taken into account in the interferogram and hence the total number of pixels $N_{\rm pix}$ read on the detector. We impose in this section $N_{\rm pattern} = 2$. This choice means that the detector reading window is two mode patterns wide, exactly as if we only would consider the fringes in the first lobe of the diffraction pattern, in the case of an Airy disc. Such choice seems reasonable at first thought because outside this lobe the interferogram is severely attenuated (as one can notice in Fig. 2). Nevertheless, a deeper analysis of this specific point shows that such a parameter is a key issue, as will be discussed in Section 4.2.

(v) The fraction of flux going into the photometric channels (i.e. the transmission of the beam splitter). We assume here that the beam splitter selects 30 per cent of the flux for the photometry.

For a given source magnitude, the number of photoevents occurring on each pixel of the interferometric and the photometric channels are computed following equations (3) and (4) respectively, assuming photon noise and additive detector noise with $\sigma = 15\,{\rm e}^-\,{\rm pixel}^{-1}$. Such a procedure is then repeated until we obtain a sample of 1000 data sets, which is large enough to perform statistics. For both estimators, we compute the theoretical and statistical mean value and S/N of the modal visibility $|\widetilde{V^{ij}}|^2$, using equations (5) and (18). Fig. 3 shows the results of our computations, for both methods (formal and simulated) and for both estimators (P2VM and Fourier), setting the true value of the modal visibility to 0.5. Theoretical calculations and numerical simulations are in excellent agreement, both for the estimated visibility and the S/N. This study validates the theoretical expressions of both estimators as well as their respective theoretical S/N.

4 DISCUSSION

4.1 Estimator relative performances

Although both estimators arise from the same formal definition of equation (5), they exhibit fundamental conceptual differences.

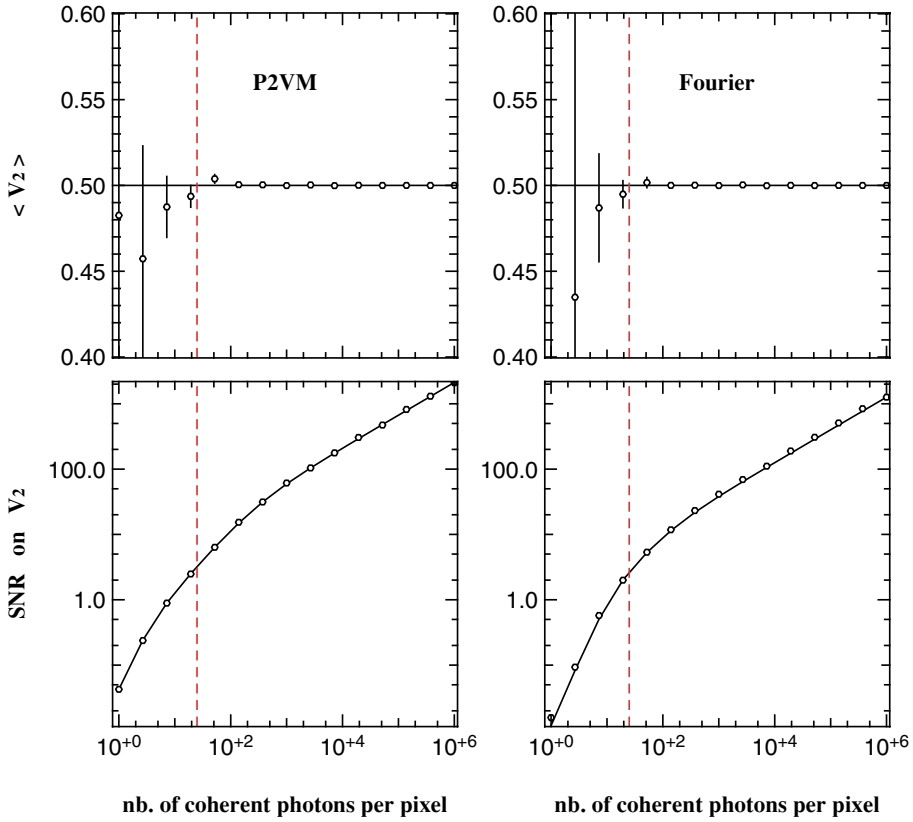

Figure 3. Theoretical (solid lines) and simulated (cross) values of the modal visibility mean value (top) and S/N (bottom), for the P2VM (left) and the Fourier (right) estimators. Plots are shown as a function of the number of photoevents per pixel in the interferogram. Detector noise has been set to $\sigma = 15\,{\rm e}^-\,{\rm pixel}^{-1}$. The vertical dashed line shows the limit between the detector and the photon noise regime. For the estimation of the visibility arising from numerical simulations, we plot the statistical error bars due to a limited number of samples (1000 data sets), i.e. the dispersion of the 1000 estimated modal visibilities, divided by the square root of the number of samples.

Obviously, both techniques present the same instrumental contrast (see equations 9 and 17, respectively), which is not surprising because the instrumental design is strictly the same, as well as the same estimation of the photometry (see equations 7 and 13, respectively). However, the very difference lies in the computation of the coherent flux.

First, in the Fourier case, the coherent flux results in a second-order (i.e. quadratic) estimation, i.e. $|F_{\rm c}^{ij}|^2$ is directly estimated. In contrast, the model-based computation is equivalent to a first-order estimation, that is the complex quantity $F_{\rm c}^{ij}$ is calculated, and then the squared modulus is taken to get rid of the atmospheric differential piston. This latter method is equivalent to fit the complex Fourier Transform of the interferogram. A second-order estimator based on modelling would have been the fitting of the power spectral density itself, or equivalently, the fitting of the autocorrelation of the interferogram in the detector plane. Performing first-order estimation is above all interesting because it allows to separate information (i.e. the visibilities for each baseline) before computing the squared modulus. As a result, this method prevents 'cross-talk' between the baselines even if the peaks are partially superimposed, which is particularly worthwhile in the case of visibility estimation from multibeam ($\geqslant$3) interferometers, as developed in our second paper on the subject (Lebouquin & Tatulli, in preparation). We also infer that a first-order estimation drives better (or at worst identical) performances than a quadratic one, though a thorough analysis of this point, which is beyond the scope of this paper, remains to be done. Moreover and above all, the model-based algorithm, thanks to the P2VM calibration matrix, entirely benefits from knowledge of the instrument, whereas the Fourier estimator does not.[2] When making use of the model-based estimator, the shape of the interferogram is perfectly known: precisely, its envelope (the diffraction pattern $\sqrt{a_k^i a_k^j}$) as well as its coding frequency and its instrumental phase. This a priori information is gathered in the matrix $\mathbf{C}$ defined in Section 2.2. Also clearly, introducing perfectly known (i.e. true and un-noisy) a priori information in the data reduction procedures can only improve the performances of the corresponding estimator. These two remarks and particularly the second point explain why the model-based algorithm leads to better performances than the Fourier one, as is illustrated in Fig. 4. Note that the higher the visibility, the greater the S/N improvement. In the two-telescope case, a gain of a factor 3 to 5 can be achieved at best, for unresolved sources.

However, this analysis assumes perfect calibration of the instrument. It means that the calibration matrix must be both perfectly stable in time and very precise, i.e. recorded with an S/N much higher than the S/N of the interferograms. If the instrument is not stable between the calibration procedures and the observations, the P2VM will drift and, as a result, the estimated visibilities will be biased. Also, if the calibration is not precise enough, it will be the limiting factor of the visibility S/N. In the case of the AMBER instrument, the calibration procedure is quite complex and it can require a great integration time (several minutes) to get a useful and precise calibration. More generally, the time and the way to calibrate an instrument severely depends on its stability and on its complexity. Ambitious designs such as the 'silicon v-groove array' of the MIRC recombiner (Monnier et al. 2004b), or recombination schemes making use of integrated optics chips (Berger et al. 2003; Lebouquin et al. 2004) should drive drastic improvements on this specific point.

[2]Although some approximate assumptions about the peak position have to be made to set the integration interval.

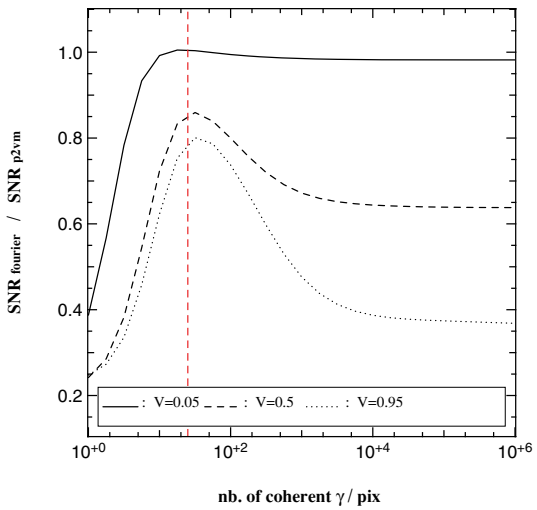

Figure 4. Ratio between the S/N of the Fourier estimator and the S/N of the model-based one, as a function of the number of photoevents per pixel in the interferogram. Detector noise is still $\sigma = 15\,{\rm e}^-$ pixel^{-1}. The curves are plotted for three types of sources: fully resolved ($V = 0.05$, solid line), moderately resolved ($V = 0.5$, dashed line) and unresolved ($V = 0.95$, dotted line).

4.2 Influence of instrumental parameters

Previous analysis has been done with a given configuration of the instrument. One last point to investigate is how both estimators behave, one compared to the other, when the parameters governing the interferogram are varying. Obviously, modifying the number of pixels per fringe or even the detector noise level will result in similar changes for both estimators, i.e. the slope of the S/N in the detector noise regime. Also, changing the coding frequency, which only defines the position of the interferometric peak in the Fourier space, will lead to equivalent modifications of the performances of both estimators, at least as far as the high-frequency peaks are separable.[3] At last, choosing the optimized area on which the interferogram gives valuable information without adding too much detector noise is a crucial point. Because the model-based algorithm takes into account the shape of the interferogram whereas the Fourier estimator does not, the compromise to find is not the same in both cases. It means the response to a change of the detector reading window will differ with regards to the chosen estimator. The effects of this parameter are investigated here.

In a multi-axial combination, one has the choice of the limits of the reading window on the detector, i.e. of the number of pixels to consider. Also, the larger the window, the more signal you integrate, but the more detector noise you record too. In Fig. 5, we show the evolution of the S/N of the modal visibility as a function of the width of the window on the detector (here defined in the fraction of intensity mode pattern). The entire first lobe of the fringe pattern contains $N_{\rm fri} = 8$ fringes, with $N_{\rm pf} = 4$ pixels per fringe. All the other parameters of the instrument are kept unchanged.

(i) Fourier estimator: in the photon-poor regime, at the detection limit of the instrument, the S/N shows a maximum when the width of the reading window is about half of the first lobe of the envelope. Beyond that point, the pixels have very small individual S/N and only bring a noise contribution in the estimation of the visibility. In

[3]When $N_{\rm tel} \geqslant 3$, see Lebouquin & Tatulli (in preparation).

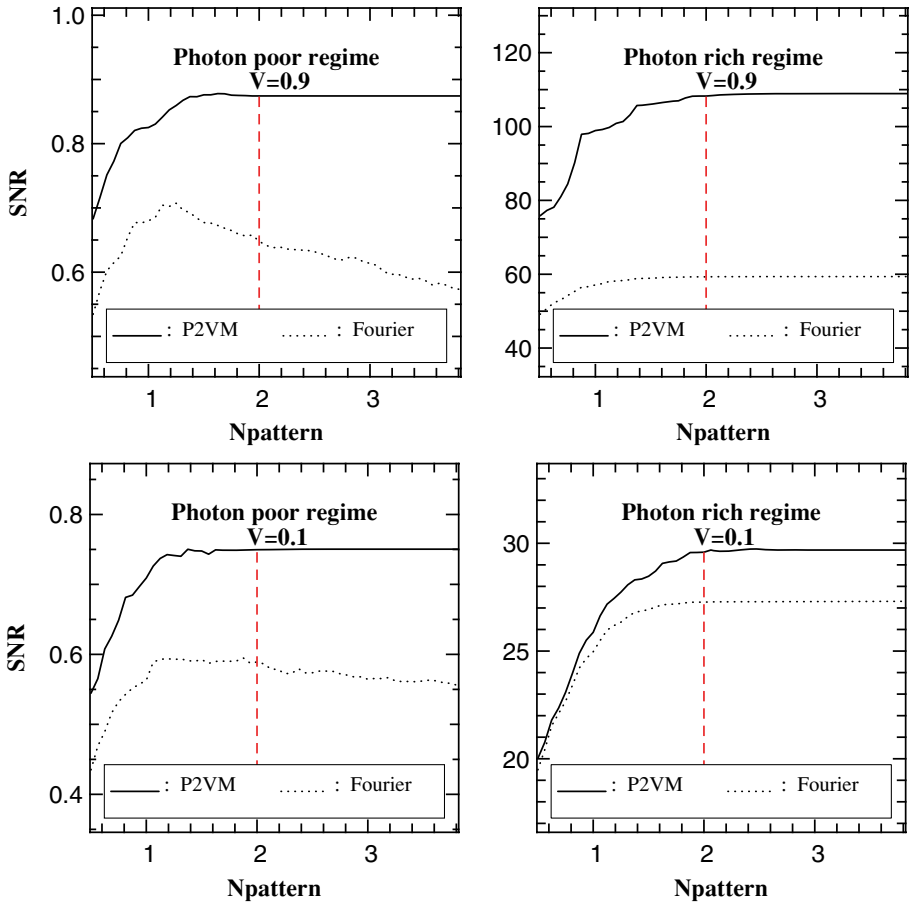

Figure 5. S/N of the modal visibility as a function of the detector reading window, in the fraction of intensity mode pattern, for photon-poor (left, here 1γ pixel^{-1}) and photon-rich (right, here 10^6 γ pixel^{-1}) regimes. Results are displayed for marginally resolved ($V = 0.9$, top) and fully resolved ($V = 0.1$, bottom) sources. The instrumental parameters are: $N_{\rm fri} = 4$ fringes per beam, $N_{\rm pf} = 4$ pixels per fringe, and a detector noise of $\sigma = 15\,{\rm e}^-$ pixel^{-1}. The vertical dashed lines correspond to recording one entire mode pattern (see Fig. 2).

the photon-rich regime, the S/N reaches its maximum for the same width of the reading window but exhibits a plateau as the width increases. This behaviour continues for as long as the S/N of each individual pixel is dominated by the photon noise. Then the S/N of the visibility starts to decrease. The width of the plateau depends on the incoming flux of the source and is all the more large than the source is bright.

(ii) Model-based estimator: as for the Fourier estimator, the shape of the S/N for the model-based estimator is linked to the shape of the fringe pattern. However, in this case, the S/N is increasing with the width of the detector window and does not exhibit a maximum (in other words, the optimum is found for an 'infinite' width). As a matter of fact, thanks to the generalized inverse of the matrix **C** that takes into account the shape of the interferogram, each pixel contribution is weighted by its individual S/N. So the pixels with bad S/N (due to the envelope or fringe modulation) are 'removed' from the reconstruction and do not introduce noise into the estimation of the visibility. Nevertheless, we can see that the slope of the S/N becomes almost flat from a detector width of about one intensity mode pattern.

This analysis shows that, in the framework of interferometric observations making use of multi-axial all-in-one recombination and in the case of bright sources, it is worth the effort integrating the interferogram on the entire lobe in order to optimize the S/N of the visibility. This statement stands for both estimators. When observing faint sources, i.e. when reaching the limiting magnitude of the instrument, and in the specific case of the Fourier estimator, performances are slightly improved when reducing the width of the reading window to half of the lobe, although the gain on the S/N never exceeds a factor of 2.

5 CONCLUSION

In this paper, we have developed the theoretical formalism that allows to model single-mode interferometers using multi-axial all-in-one coding, from the signal processing point of view. From this formalism, two estimators of the visibility have been analysed. The first one consists of using the classical integration of the power spectral density of the interferogram in the Fourier plane, whereas the second one deals with modelling the interferogram in the detector plane, as has been chosen for the AMBER experiment. Performances of such estimators have been computed. Considering photon and detector noises, theoretical expression of the S/N of the visibility have been recalled for the Fourier estimator, and derived for the first time in the case of the model-based estimator. These expressions have been validated through numerical simulations and then compared. We have shown that the second technique offers optimal performances

because it makes full use of knowledge about the instrument, especially the shape of the interferogram. In the two-telescope case that has been emphasized in this paper, we have demonstrated that the model-based estimator enables at best to achieve over a factor of 5 of the visibility S/N, compared to the Fourier one. Finally, we have addressed the question of the width of the reading window of the detector. This point is indeed a crucial issue when dealing with multi-axial recombination. We have shown that, regardless of the chosen estimator, integrating the entire lobe of the intensity mode pattern offers optimized performances.

ACKNOWLEDGMENTS

The authors thank Drs K. Perrault and F. Malbet for very helpful suggestions that improved the presentation of the paper. They wish also to thank the referee for careful reading of this work and for subsequent comments that improved the clarity of this paper. All the calculations and graphics were performed with the freeware YORICK.[4]

REFERENCES

Baldwin J. E. et al., 1996, A&A, 306, L13
Berger J. et al., 2003, Proc. SPIE, 4838, 1099
Colavita M. M., 1999, PASP, 111, 111
Conan J.-M., 1994, PhD thesis, Univ. Paris XI Orsay
Coudé du Foresto V., Faucherre M., Hubin N., Gitton P., 2000, A&AS, 145, 305
Coudé Du Foresto V., Ridgway S., Mariotti J.-M., 1997, A&AS, 121, 379
Goodman J. W., 1985, Statistical Optics. Wiley, New York
Högbom J. A., 1974, A&AS, 15, 417
Hummel C. A., 1998, Proc. SPIE, 3350, 483
Lebouquin J.-B. et al., 2004, Proc. SPIE, 5491, 1362
Malbet F. et al., 2004, Proc. SPIE, 5491, 439
Mège P., Malbet F., Chelli A., 2001, in Combes F., Barret D., Thévenin F., eds, SF2A-2001: Semaine de l'Astrophysique Francaise. EDP Sciences, Lyon, p. 581
Millour F., Tatulli E., Chelli A. E., Duvert G., Zins G., Acke B., Malbet F., 2004, Proc. SPIE, 5491, 1222
Monnier J. D. et al., 2004a, ApJ, 602, L57
Monnier J. D. et al., 2004b, Proc. SPIE, 5491, 1370
Papoulis A., 1984, Probability, random variables and stochastic processes, 2nd edn. McGraw-Hill, New York
Perrin G., 2003, A&A, 398, 385
Petrov R. G. et al., 2000, Proc. SPIE, 4006, 68
Roddier F., Lena P., 1984, J. Opt., 15, 171
Shaklan S., Roddier F., 1988, Appl. Opt., 27, 2334
Tatulli E., Chelli A., 2005, J. Opt. Soc. Am. A, 22, 1589
Tatulli E., Thiébaut E., Malbet F., Duvert G., 2004a, Proc. SPIE, 5491, 117
Tatulli E., Mège P., Chelli A., 2004b, A&A, 418, 1179
Thiébaut E., Garcia P. J. V., Foy R., 2003, Ap&SS, 286, 171
Tuthill P. G., Monnier J. D., Danchi W. C., 2000, Proc. SPIE, 4006, 491
Young J. S. et al., 2000, MNRAS, 315, 635

APPENDIX A: THEORETICAL S/N OF THE VISIBILITY

We assume that the interferogram as well as the photometric outputs are corrupted by photon (Poisson) noise and additive Gaussian noise of variance σ^2.

[4]ftp://ftp-icf.llnl.gov/pub/Yorick/doc/index.html

A1 Generic expression

The estimator of the squared visibility can be expressed in a generic form

$$\widetilde{|V^{ij}|^2} \propto \frac{\left\langle \left|F_c^{ij}\right|^2 \right\rangle}{\langle F^i F^j \rangle}, \tag{A1}$$

where F_c^{ij} is the coherent flux at the frequency f^{ij}, and F^i, F^j are the photometric fluxes.

The relative error $\mathcal{E}(|V^{ij}|^2)$ on the squared visibility is then given by Papoulis (1984):

$$\begin{aligned}\mathcal{E}^2(|V^{ij}|^2) = {} & \frac{\sigma^2\left(\left|F_c^{ij}\right|^2\right)}{\overline{\left|F_c^{ij}\right|^2}^2} + \frac{\sigma^2(F^i)}{\overline{F^i}^2} + \frac{\sigma^2(F^j)}{\overline{F^j}^2} \\ & + 2\frac{\mathrm{Cov}(F^i, F^j)}{\overline{F^i F^j}} \\ & - 2\frac{\mathrm{Cov}\left(\left|F_c^{ij}\right|^2, F^i F^j\right)}{\overline{\left|F_c^{ij}\right|^2}\,\overline{F^i F^j}}.\end{aligned} \tag{A2}$$

Theoretical expression of each term of the previous equation is now given for both estimators.

A2 S/N for the Fourier estimator

The coherent flux is linked to the spectral density of the interferogram by the following relationship (see equation 6, written in its sampled form):

$$\left|F_c^{ij}\right|^2 \propto \sum_k \left|\widehat{M}^{ij}(f_k)\right|^2. \tag{A3}$$

Hence, the expected value and the error on the coherent flux is written as

$$\overline{\left|F_c^{ij}\right|^2} \propto \sum_k \overline{\left|\widehat{M}^{ij}(f_k)\right|^2}, \tag{A4}$$

$$\begin{aligned}\sigma^2\left(\left|F_c^{ij}\right|^2\right) \propto {} & \sum_k \sigma^2\left(\left|\widehat{M}^{ij}(f_k)\right|^2\right) \\ & + \sum_k \sum_{l\neq k} \mathrm{Cov}\left(\left|\widehat{M}^{ij}(f_k)\right|^2, \left|\widehat{M}^{ij}(f_l)\right|^2\right).\end{aligned} \tag{A5}$$

The statistics of the spectral density of an interferogram have already been computed by Goodman (1985) in the case of photon noise and completed by Tatulli et al. (2004b) with detector and atmospheric noise. We recall the results here, without taking into account the atmospheric noise (i.e. speckle noise):

$$\overline{\left|\widehat{M}^{ij}(f_k)\right|^2} = \overline{N}^2\left|\widehat{i}(f_k)\right|^2 + \overline{N} + N_{\mathrm{pix}}\sigma_{\mathrm{det}}^2, \tag{A6}$$

where we recognize the bias part due to photon noise ($\overline{N}$, Goodman 1985) and additive Gaussian noise ($N_{\mathrm{pix}}\,\sigma_{\mathrm{det}}^2$, Tatulli et al. 2004b),

$$\begin{aligned}\sigma^2(|\widehat{M}^{ij}(f_k)|^2) = {} & 2\overline{N}^3|\widehat{i}(f_k)|^2 + 4\overline{N}^2|\widehat{i}(f_k)|^2 + \overline{N}^2 \\ & + N_{\mathrm{pix}}^2\sigma^4 + 3N_{\mathrm{pix}}\sigma^4 + 2N_{\mathrm{pix}}\sigma^2\overline{N} \\ & + 2N_{\mathrm{pix}}\sigma^2\overline{N}^2|\widehat{i}(f_k)|^2,\end{aligned} \tag{A7}$$

$$\begin{aligned}\mathrm{Cov}\left(\left|\widehat{M}^{ij}(f_k)\right|^2, \widehat{M}^{ij}(f_l)\right|^2) = {} & 2\overline{N}^3\mathrm{Re}[\widehat{i}(f_k)\widehat{i}^*(f_l)\widehat{i}^*(f_k - f_l)] \\ & + 2\overline{N}^3\mathrm{Re}[\widehat{i}(f_k)\widehat{i}(f_l)\widehat{i}^*(f_k + f_l)] \\ & + 2\overline{N}^2|\widehat{i}(f_k)|^2 \\ & + 2\overline{N}^2|\widehat{i}(f_l)|^2 \\ & + \overline{N}^2|\widehat{i}(f_k - f_l)|^2 \\ & + \overline{N}^2|\widehat{i}(f_k + f_l)|^2 \\ & + \overline{N} + 3N_{\mathrm{pix}}\sigma^4, \end{aligned} \tag{A8}$$

where $\widehat{i}(f)$ is the normalized spectral density [such as $\widehat{i}(0) = 1$], i.e.

$$\widehat{i}(f) = V(f)\widehat{g}(f), \tag{A9}$$

$$\widehat{i}(f) = \frac{V(f)}{N_{\mathrm{tel}}}\widehat{g}(f), \tag{A10}$$

for the photometric and the interferometric peaks respectively, N_{tel} being the number of telescopes, and $\widehat{g}(f)$ being the normalized Fourier Transform of the beam $a(\alpha)$ (assuming, the same shape for the whole beams). Furthermore, we have

$$\sigma^2(F^i) = \overline{F^i} + \sigma^2_{\mathrm{det}}. \tag{A11}$$

Finally, because the coherent flux and each photometric flux are estimated independently, we have

$$\mathrm{Cov}\left(\left|F_{\mathrm{c}}^{ij}\right|^2, F^iF^j\right) = 0, \tag{A12}$$

$$\mathrm{Cov}(F^i, F^j) = 0. \tag{A13}$$

A3 S/N for the P2VM estimator

We recall that the real and imaginary part of the weighted complex visibility are defined by the system of equations

$$\begin{bmatrix} i \\ P \end{bmatrix} = [\mathbf{C}] \begin{bmatrix} R \\ I \\ F \end{bmatrix}. \tag{A14}$$

If we call $\boldsymbol{M} = m_k, k \in [1..N_{\mathrm{pix}} + N_{\mathrm{tel}}]$ the vector resulting in the concatenation of the interferogram i and the photometry P, we can write

$$R^{ij} = \sum_k^{N_{\mathrm{pix}}} \xi_k^{ij} m_k, \tag{A15}$$

$$I^{ij} = \sum_k^{N_{\mathrm{pix}}} \zeta_k^{ij} m_k, \tag{A16}$$

$$F^i = \sum_k^{N_{\mathrm{pix}}} \beta_k^i m_k, \tag{A17}$$

where ξ_k^{ij}, ζ_k^{ij} and β_k^i are the coefficients of the P2VM matrix. Hence, one obtains

$$\left|F_{\mathrm{c}}^{ij}\right|^2 = R^{ij^2} + I^{ij^2} = \sum_k \sum_l \left[\xi_k^{ij}\xi_l^{ij} + \zeta_k^{ij}\zeta_l^{ij}\right] m_k m_l, \tag{A18}$$

$$F^iF^j = \sum_k \sum_l \beta_k^i \beta_l^j m_k m_l. \tag{A19}$$

Here, the covariance between the coherent flux and the photometric fluxes, as well as the covariance between the photometric fluxes, have to be taken into account. For the sake of simplicity, equation (A2) can be rewritten:

$$\begin{aligned}\mathcal{E}^2(|V^{ij}|^2) = {} & \frac{\sigma^2\left(\left|F_{\mathrm{c}}^{ij}\right|^2\right)}{\overline{\left|F_{\mathrm{c}}^{ij}\right|^2}^2} + \frac{\sigma^2(F^iF^j)}{\overline{F^iF^j}^2} \\ & - 2\frac{\mathrm{Cov}\left(\left|F_{\mathrm{c}}^{ij}\right|^2, F^iF^j\right)}{\overline{\left|F_{\mathrm{c}}^{ij}\right|^2}\,\overline{F^iF^j}}. \end{aligned} \tag{A20}$$

It now remains to compute all the terms knowing that

$$\sigma^2\left(\left|F_{\mathrm{c}}^{ij}\right|^2\right) = \overline{\left|F_{\mathrm{c}}^{ij}\right|^4} - \overline{\left|F_{\mathrm{c}}^{ij}\right|^2}^2, \tag{A21}$$

$$\sigma^2(F^iF^j) = \overline{F^{i^2}F^{j^2}} - \overline{F^iF^j}^2, \tag{A22}$$

$$\mathrm{Cov}\left(\left|F_{\mathrm{c}}^{ij}\right|^2, F^iF^j\right) = \overline{\left|F_{\mathrm{c}}^{ij}\right|^2 F^iF^j} - \overline{\left|F_{\mathrm{c}}^{ij}\right|^2}\,\overline{F^iF^j}. \tag{A23}$$

To lighten the calculations, we introduce the variable γ such that $\gamma_{kl}^{ij} = \xi_k^{ij}\xi_l^{ij} + \zeta_k^{ij}\zeta_l^{ij}$. Then we can compute the second-order statistics of the squared coherent flux and the photometric fluxes:

$$\begin{aligned}\overline{\left|F_{\mathrm{c}}^{ij}\right|^2} &= \sum_k \sum_l \gamma_{kl}^{ij}\overline{m_k m_l} \\ &= \sum_k \gamma_{kk}^{ij}\overline{m_k^2} + \sum_k \sum_{l\neq k} \gamma_{kl}^{ij}\overline{m_k}\,\overline{m_l}, \end{aligned} \tag{A24}$$

$$\overline{F^iF^j} = \sum_k \beta_k^i\beta_k^j\overline{m_k^2} + \sum_k \sum_{l\neq k} \beta_k^i\beta_l^j\overline{m_k}\,\overline{m_l}. \tag{A25}$$

Then the fourth-order statistics $\overline{F^4} = \overline{|F_{\mathrm{c}}^{ij}|^4}, \overline{F^{i^2}F^{j^2}}, \overline{|F_{\mathrm{c}}^{ij}|^2F^iF^j}$ can be described by the generic equation

Table A1. Coefficients of the fourth-order statistics of the coherent and photometric fluxes: (a) $|F_{\mathrm{c}}^{ij}|^4$ and $F^{i^2}F^{j^2}$; (b) $|F_{\mathrm{c}}^{ij}|^2F^iF^j$.

(a)	$\overline{\lvert F_{\mathrm{c}}^{ij}\rvert^4}$	$\overline{F^{i^2}F^{j^2}}$
$\alpha_{k,l,n,o}^{(1)}$	$\gamma_{kl}^{ij}\,\gamma_{no}^{ij}$	$\beta_k^i\beta_l^j\beta_n^i\beta_o^j$
$\alpha_{kln}^{(2,1,1)}$	$2\gamma_{kk}^{ij}\,\gamma_{ln}^{ij} + 4\gamma_{kl}^{ij}\,\gamma_{kn}^{ij}$	$\beta_k^{i^2}\beta_l^j + \beta_k^{j^2}\beta_l^i\beta_n^i + 4\,\beta_k^i\beta_k^j\,\beta_l^i\,\beta_n^j$
$\alpha_{kl}^{(2,2)}$	$\gamma_{kk}^{ij}\,\gamma_{ll}^{ij} + 2\gamma_{kl}^{ij}\,\gamma_{kl}^{ij}$	$\beta_k^{i^2}\beta_l^{j^2} + \beta_k^i\beta_l^i\beta_k^j\beta_l^j$
$\alpha_{kl}^{(3)}$	$4\gamma_{kk}^{ij}\,\gamma_{kl}^{ij}$	$2\beta_k^{i^2}\beta_k^j\beta_l^j + 2\beta_k^{j^2}\beta_k^i\beta_l^i$
$\alpha_k^{(4)}$	$\gamma_{kk}^{ij}\,\gamma_{kk}^{ij}$	$\beta_k^{i^2}\beta_k^{j^2}$
(b)	$\overline{\lvert F_{\mathrm{c}}^{ij}\rvert^2F^iF^j}$	
$\alpha_{k,l,n,o}^{(1)}$	$\gamma_{kl}^{ij}\,\beta_n^i\,\beta_o^j$	
$\alpha_{kln}^{(2,1,1)}$	$\gamma_{kk}^{ij}\,\beta_l^i\beta_n^j + \gamma_{ln}^{ij}\,\beta_k^i\beta_k^j + 2\gamma_{kl}^{ij}\,[\beta_k^i\beta_n^j + \beta_n^i\beta_k^j]$	
$\alpha_{kl}^{(2,2)}$	$\gamma_{kk}^{ij}\,\beta_l^i\beta_l^j + \gamma_{kl}^{ij}\,[\beta_k^i\beta_l^j + \beta_l^i\beta_k^j]$	
$\alpha_{kl}^{(3)}$	$\gamma_{kk}^{ij}\,[\beta_k^i\beta_l^j + \beta_l^i\beta_k^j] + 2\gamma_{kl}^{ij}\,\beta_k^i\beta_k^j$	
$\alpha_k^{(4)}$	$\gamma_{kk}^{ij}\,\beta_k^i\beta_k^j$	

$$\begin{aligned}\overline{F^4} = &\sum_k \alpha_k^{(4)} \overline{m_k^4} + \sum_k \sum_{l\neq k} \alpha_{kl}^{(3)} \overline{m_k^3}\,\overline{m_l} \\ &+ \sum_k \sum_{l\neq k} \alpha_{kl}^{(2,2)} \overline{m_k^2}\,\overline{m_l^2} \\ &+ \sum \sum_{l\neq k\neq n} \sum \alpha_{kln}^{(2,1,1)} \overline{m_k^2}\,\overline{m_l}\,\overline{m_n} \\ &+ \sum \sum_{l\neq k} \sum_{\neq o\neq n} \sum \alpha_{klno}^{(1)} \overline{m_k}\,\overline{m_l}\,\overline{m_n}\,\overline{m_o}, \end{aligned} \tag{A26}$$

where $\alpha_{klno}^{(1)}$, $\alpha_{kln}^{(2,1,1)}$, $\alpha_{kl}^{(2,2)}$, $\alpha_{kl}^{(3)}$ and $\alpha_k^{(4)}$ are given in Table A1 in each specific case. Previous equations can be computed knowing the statistics of m_k, i.e.

$$\overline{m_k^2} = \overline{m_k}^2 + \overline{m_k} + \sigma^2, \tag{A27}$$

$$\overline{p^2} = \overline{p}^2 + \overline{p} + N_{\rm photpix}\sigma^2, \tag{A28}$$

$N_{\rm photpix}$ being the number of pixels to code the photometric outputs. The third and fourth moments $\overline{m_k^3}$ and $\overline{m_k^4}$ are derived from first- and second-order ones assuming Gaussian statistics for the sake of simplicity.

This paper has been typeset from a TEX/LATEX file prepared by the author.